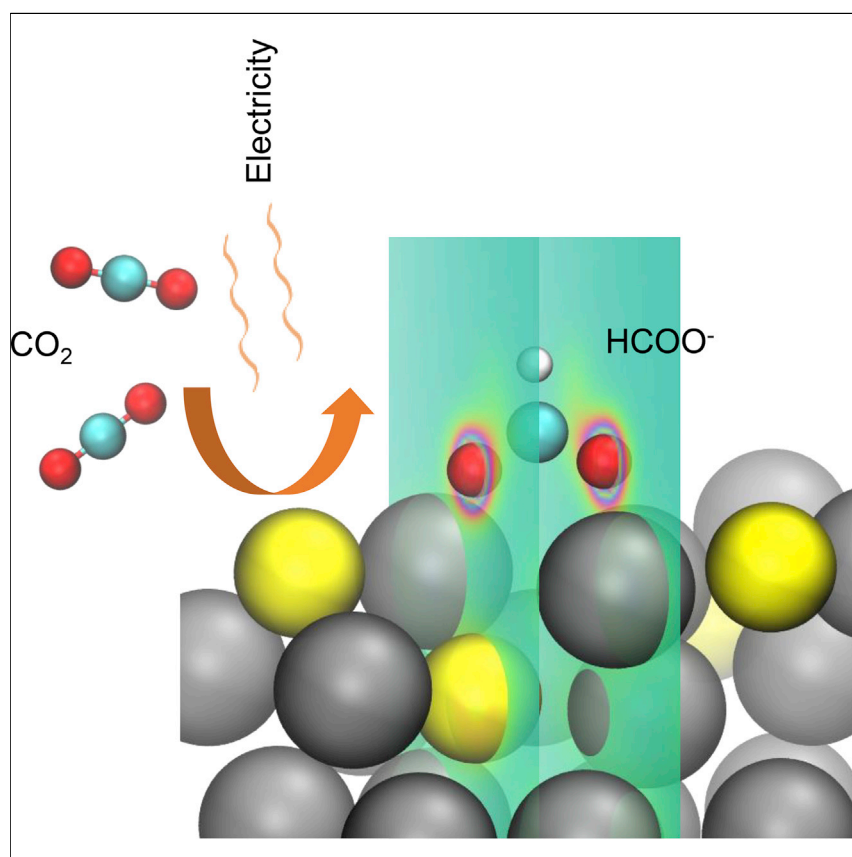


Article

Sulfur-Modulated Tin Sites Enable Highly Selective Electrochemical Reduction of CO₂ to Formate

The electrochemical reduction of carbon dioxide (CO₂RR) offers a compelling route to energy storage and high-value chemical manufacture. The presence of sulfur atoms in catalyst surfaces promotes undercoordinated sites, thereby improving the electrochemical reduction of CO₂ to formate. The resulting sulfur-modulated tin catalysts accelerate CO₂RR at geometric current densities of 55 mA cm⁻² at -0.75 V versus RHE with a Faradaic efficiency of 93%.

Xueli Zheng, Phil De Luna, F. Pelayo García de Arquer, ..., Xiwen Du, Peidong Yang, Edward H. Sargent

ted.sargent@utoronto.ca

HIGHLIGHTS

Electrochemical reduction of CO₂ to renewable fuels is urgently needed

The incorporation of sulfur into tin favors formate generation

Sulfur-modulated tin increases the CO₂ reduction current density

Sulfur-modulated tin provides excellent stability

Article

Sulfur-Modulated Tin Sites Enable Highly Selective Electrochemical Reduction of CO₂ to Formate

Xueli Zheng,^{1,2,6,9} Phil De Luna,^{3,4,9} F. Pelayo García de Arquer,¹ Bo Zhang,¹ Nigel Becknell,⁴ Michael B. Ross,⁴ Yifan Li,^{4,7} Mohammad Norouzi Banis,⁵ Yuzhang Li,⁶ Min Liu,¹ Oleksandr Voznyy,¹ Cao Thang Dinh,¹ Taotao Zhuang,¹ Philipp Stadler,⁸ Yi Cui,⁶ Xiwen Du,² Peidong Yang,^{4,7} and Edward H. Sargent^{1,10,*}

SUMMARY

Electrochemical reduction of carbon dioxide (CO₂RR) to formate provides an avenue to the synthesis of value-added carbon-based fuels and feedstocks powered using renewable electricity. Here, we hypothesized that the presence of sulfur atoms in the catalyst surface could promote undercoordinated sites, and thereby improve the electrochemical reduction of CO₂ to formate. We explored, using density functional theory, how the incorporation of sulfur into tin may favor formate generation. We used atomic layer deposition of SnS_x followed by a reduction process to synthesize sulfur-modulated tin (Sn(S)) catalysts. X-ray absorption near-edge structure (XANES) studies reveal higher oxidation states in Sn(S) compared with that of tin in Sn nanoparticles. Sn(S)/Au accelerates CO₂RR at geometric current densities of 55 mA cm⁻² at -0.75 V versus reversible hydrogen electrode with a Faradaic efficiency of 93%. Furthermore, Sn(S) catalysts show excellent stability without deactivation (<2% productivity change) following more than 40 hours of operation.

INTRODUCTION

The electrochemical reduction of carbon dioxide (CO₂RR) offers a compelling route to energy storage and high-value chemical manufacture.¹⁻⁴ It enables the use of increasingly abundant renewable energy sources, such as solar and wind, to drive the conversion of CO₂ to renewable fuels and feedstocks. This approach stands to reduce present-day dependence on conventional fuels and also help mitigate net CO₂ emissions. Despite recent breakthroughs, the energy efficiency of CO₂RR is still far from being a viable alternative to fossil energy sources.⁴⁻⁷ Improvements in selectivity and partial current density with robust and stable long operating times are of crucial importance to continue advances in the direction of commercial viability.

Formate is one interesting product among the variety that can be synthesized via CO₂RR. It can be directly used as a fuel, as a means of H₂ storage, or as a feedstock in the synthesis of fine chemicals of interest to the pharmaceutical industry.^{8,9} A recent paper utilizing a gross-margin model for defining techno-economic benchmarks for CO₂ reduction showed that formate and carbon monoxide may offer paths to economically viable products.¹⁰ Unfortunately, in the case of formate, high selectivity has been achieved only at the expense of low current density, yielding

Context & Scale

With rapid advances in the efficient and cost-effective conversion of sunlight to electrical power, the development of storage technologies for renewable energy is even more urgent. Using renewable electricity to convert CO₂ into formate simultaneously addresses the need for storage of intermittent renewable energy sources and the need to reduce greenhouse gas emissions. We report an increase of greater than 4-fold in the current density (hence the rate of reaction) in formate electrosynthesis compared with relevant controls. Our catalysts also show excellent stability without deactivation (<2% productivity change) following more than 40 hours of operation.

impractically low partial current densities (j_{HCOO^-}). In addition, many catalysts exhibit rapid deactivation within hours.^{4,11–15}

Metal surfaces have been widely used for the heterogeneous electroreduction of CO₂ due to their robustness and superior catalytic activity.^{6,14,16} Different strategies have been explored to control selectivity, reduce overpotentials, and increase energy efficiency.^{17–26} From a materials perspective, the choice of metals can be used to tailor CO₂RR selectivity. For example, metals such as Pd, Pb, Co, Hg, In, Bi, Cd, or Sn have been reported to favor selectivity toward formate over carbon monoxide or hydrogen.^{4,13,17–24} On the other hand, it has been shown that the presence of high-index facets, undercoordinated sites, and adatoms can improve CO₂RR energetics as the energy required for the intermediate steps in the electroreduction of CO₂ is lowered.^{25–27}

The use of metal-oxide-derived catalysts has been found to increase performance in CO₂ reduction when compared with their fully reduced counterparts.^{4,12,21} Metal electrodes obtained from the reduction of metal oxides exhibit a prominent increase in selectivity and provide lower overpotentials in the electrosynthesis of CO and ethylene.²⁸ This is ascribed to a combination of an increased number of undercoordinated sites, the presence of oxygen promoters in metal oxides, and the synergetic effect between remaining oxide species and native metal atoms.^{4,21,28}

Here, we demonstrate the use of sulfide-derived metal catalysts to promote a high number of favorable catalytic sites. We obtain, as a result, high selectivity and high partial current density for CO₂RR to formate. We hypothesized that sulfur-modulated tin catalysts (Sn(S)) could offer superior catalytic selectivity, since the removal of sulfur atoms incorporated in the Sn slab leads to a surface lattice distortion, thereby generating undercoordinated active Sn sites. We developed a materials strategy based on atomic layer deposition that combines ultra-sharp features—which enable exploitation of field-induced reagent concentration (FIRC)³—with the benefits of a tin sulfide-derived catalyst. As a result, we report high current density to geometric formate ($\sim 55 \text{ mA cm}^{-2}$). The new catalysts exhibit excellent stability over the course of a 40-hr initial study.

RESULTS AND DISCUSSION

Computational Studies

We first sought to model the effect on the catalytic activity of CO₂RR to formate provided by doping sulfur atoms into Sn slabs. To this end, we carried out a computational study in which we systematically varied the sulfur content from pure tin to tin(II) sulfide. Density functional theory (DFT) calculations were used to probe the energetics along the different CO₂RR pathways toward formate, carbon monoxide, and hydrogen. Different sulfur contents are expected to modify the surface morphology and electronic structure thereby affecting the CO₂RR activity (Figure S1). The electrochemical reduction of CO₂ to formate is known to proceed via an initial proton-coupled electron transfer to form a bound formate intermediate (HCOO*²⁵). Other competing reaction pathways have different predominant intermediates. Carbon monoxide evolution, for example, typically proceeds via a bound carboxylate intermediate (COOH*^{3,29}). The hydrogen evolution reaction (HER), on the other hand, requires a bound proton (H*) intermediate.³⁰

A highly selective catalyst for the production of formic acid will favor the formation of formate over carboxylate and proton intermediates. To assess the selectivity and

¹Department of Electrical and Computer Engineering, University of Toronto, 35 St George Street, Toronto, ON M5S 1A4, Canada

²Institute of New-Energy Materials, School of Materials Science and Engineering, Tianjin University, Tianjin 300072, China

³Department of Materials Science and Engineering, University of Toronto, 184 College Street, Toronto, ON M5S 3E4, Canada

⁴Department of Chemistry, University of California, Berkeley, Berkeley, CA 94720, USA

⁵Canadian Light Source, Inc.(CLS), 44 Innovation Boulevard, Saskatoon, SK S7N 2V3, Canada

⁶Department of Material Science and Engineering, Stanford University, Stanford, CA 94305, USA

⁷Chemical Sciences Division, Lawrence Berkeley National Laboratory, Berkeley, CA 94720, USA

⁸Institute of Physical Chemistry, Johannes Kepler University Linz, Altenberger Strasse 69, 4040 Linz, Austria

⁹These authors contributed equally

¹⁰Lead contact

*Correspondence: ted.sargent@utoronto.ca
<https://doi.org/10.1016/j.joule.2017.09.014>

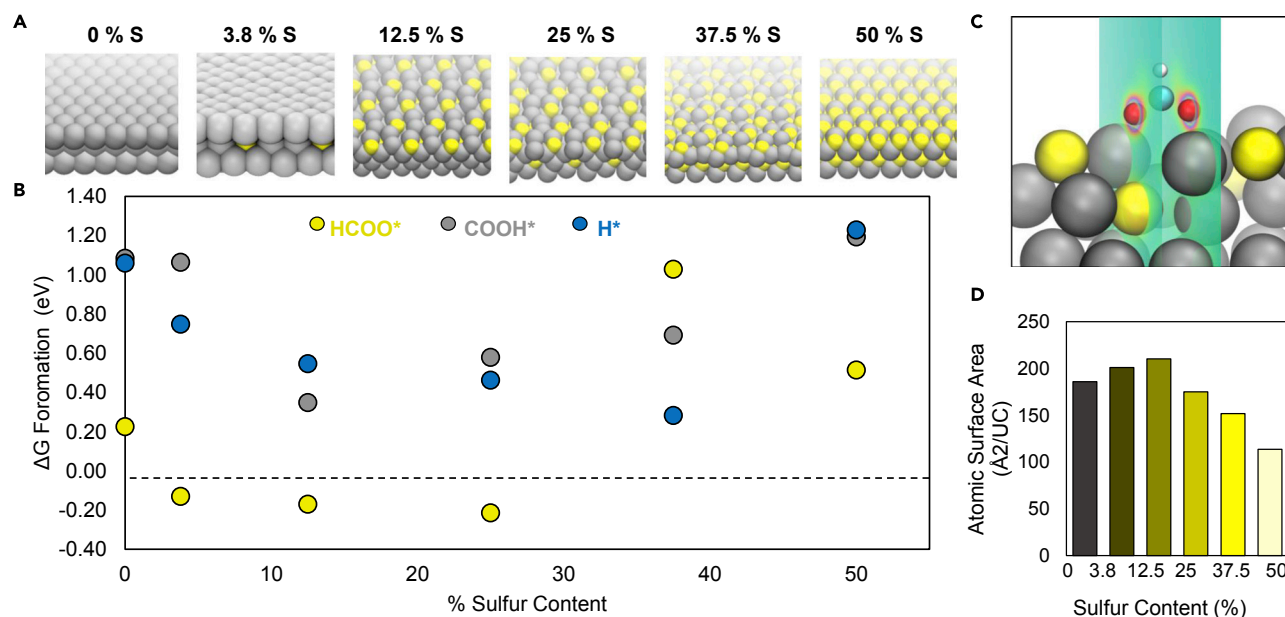


Figure 1. Computational Investigation of Sulfur-Modulated Tin System

(A) Optimized surface slab structures of pure Sn, S-modulated Sn, and SnS.

(B) Gibbs free energies of formation ($\Delta G_{\text{formation}}$) for HCOO* (yellow), COOH* (gray), and H* (blue) intermediates, which are the rate-limiting intermediates along the reaction pathway to produce formate, carbon monoxide, and hydrogen gas, respectively.

(C) Volume slice of the charge densities through the middle of the oxygen atom of a bound HCOO* intermediate.

(D) Atomic accessible surface area of the metal slab normalized to the number of tin atoms as a function of sulfur content.

limiting potentials for each product, we calculated the Gibbs free energy of formation (ΔG_f) for HCOO*, COOH*, and H* intermediates on the (100) surface of Sn(S) as a function of sulfur content (Figure 1B and Table S3). The bound HCOO* intermediate visualized with a volume slice of the electronic charge densities through the center of the oxygen atoms is shown in Figure 1C. Here, the free energy of formation is the reaction free energy necessary to electrochemically reduce CO₂ to a surface intermediate species at 0 V versus reversible hydrogen electrode (RHE) at pH 0, 298 K, and 1 atm. In the majority of cases, the Gibbs free energy of formation for HCOO* is lower than that of COOH*. This suggests that the production of formic acid is the energetically preferred pathway. The reaction energy diagram for electroreduction of CO₂ to formic acid with catalysts of various sulfur content is shown in Figure S2. For both formate and carboxylate intermediates, the same trend is observed whereby a slight doping of S into Sn drastically lowers ΔG_f and, as the content of S increases, so does the free energy of formation. An opposite trend was observed for H*, whereby the free energy of formation increases upon S incorporation.

Interestingly, the ΔG_f for HCOO* was found to be negative for 3.8% (−0.13 eV), 12.5% (−0.17 eV), and 25% (−0.21 eV) S-doped Sn. This suggests that the formation of the rate-limiting formate intermediate is thermodynamically downhill when sulfur is slightly doped into tin.

The theoretical limiting potential for CO₂RR—the calculated minimum thermodynamic potential necessary to drive the electrochemical reaction forward—was found to be closest to zero for 3.8% S with a value of −0.07 V versus RHE at pH 0, 298 K, and 1 atm (Table S4). The limiting potential is taken from the reaction energy diagram (Figure S2) and is the largest ΔG along the reaction pathway. For this same composition, the limiting potentials for CO production and HER were much more negative

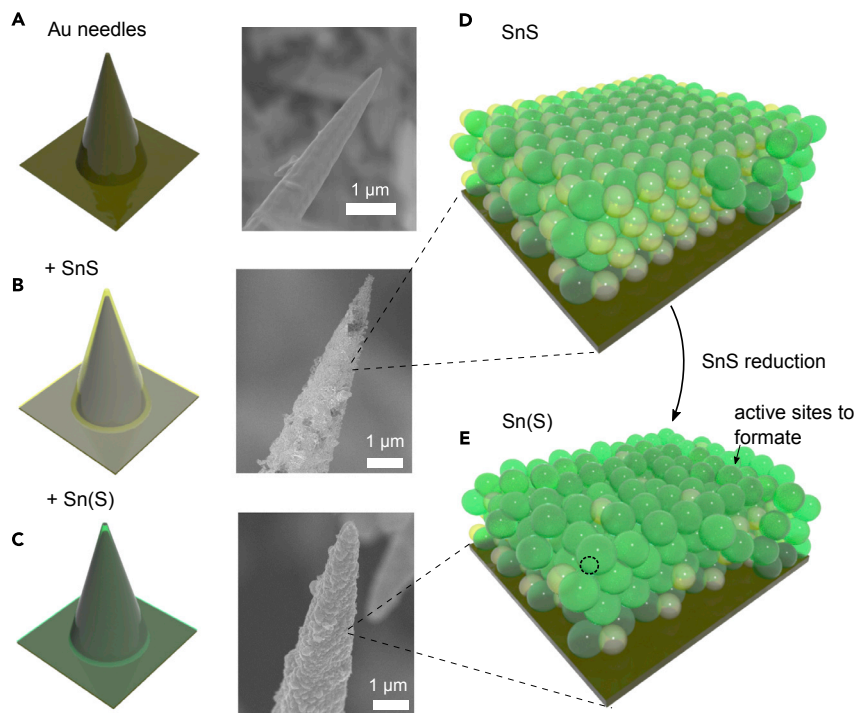


Figure 2. Fabrication of Nanostructured Sn(S) Catalysts

(A–C) Schematic and SEM images of the process leading to the fabrication of Sn(S) nanostructured electrodes. (A) Au needles. (B) Au needles after SnS deposition by ALD process. (C) Au needles coated with sulfur-modulated-tin films.

(D) A SnS_x slab is conformally deposited by ALD on top of the nanostructured metal backbone.

(E) The selective reduction of SnS_x leads to Sn(S) films, which promotes CO₂RR toward formate. The dashed circle means active sites for formate generation.

(−1.06 V and −0.75 V, respectively). These results suggest that the onset potential for formate production may be lower than that of CO or H₂, highlighting the beneficial effects of S incorporation on the energetics of formate generation.

To computationally investigate the morphological changes that doping induced on the tin, accessible surface areas were calculated using Connolly surface areas (Figure S3 and Table S6). It was found that slight doping of sulfur atoms increased the atomic surface area (normalized to the number of tin atoms in the slab) compared with tin sulfide or pure tin by 13% (Figure 1D). The 12.5% sulfur-doped Sn(S) structure had the largest accessible surface area of 210 Å² per unit cell, whereas the close-packed pure tin structure had the lowest accessible surface area of 186 Å² per unit cell. This high surface area suggests the surface has a greater degree of accessibility and is more likely to have undercoordinated sites due to the imperfect packing caused by the slight doping of sulfur. This result was validated by comparing the electrochemically active surface area (ECSA) of Sn(S) and Sn nanoparticles (NPs) as described later in the text.

Synthesis and Characterization of Sulfur-Modulated Tin Catalysts

A method to achieve a controllably sulfur-doped Sn surface was then required to successfully implement these findings. We took the view that atomic layer deposition (ALD) could provide precise control over both S content and film thickness (Figures 2 and S4). SnS_x thin films were deposited from the reaction of tetrakis(dimethylamino)tin(IV) (TDMA-Sn) and H₂S. The resulting films were then electrochemically

Table 1. Comparison of Catalytic Parameters of Sulfur-Modulated Tin Catalysts and Controls

Samples	Electrolyte	Potential (V versus RHE)	Current Density (mA cm ⁻²)	Faradaic Efficiency (%)	Reference
Sn(S)/Au	0.1 M KHCO ₃	-0.75	55	93.3	This work
Sn nanoparticles/Au	0.1 MKHCO ₃	-0.75	42	30.2	This work
SnO _x -derived Sn	0.5 M KHCO ₃	-1.05	12	19	Lu et al. ¹¹
SnO ₂ nanoparticles	0.1 M KHCO ₃	-1.05	9.5	90	Kim et al. ¹⁴
SnO _x /Sn	0.1 M KHCO ₃	-1.05	11	70	Pander et al. ²²
Oxide-derived Pb	0.5 M KHCO ₃	-1.05	1	95	Hollingsworth et al. ²³
SnS ₂ -derived Sn/rGO	0.5 M KHCO ₃	-1.05	11.75	85	Li et al. ³¹
Sn quantum sheets/GO	0.1 M KHCO ₃	-1.05	12	60	Lei et al. ³²
Partial oxidized Co	0.1 M Na ₂ SO ₄	-0.24	10	90	Gao et al. ⁴
Pd nanoparticles	0.5 M KHCO ₃	-0.20	22	97	Klinkova et al. ¹³
Pd nanoparticles	0.5 M KHCO ₃	-0.35	8	90	Won da et al. ¹⁸
Sn	[Bmim]PF ₆	-1.05	15	95	Lee et al. ¹⁶

reduced to partially remove S atoms (see [Experimental Procedures](#) for details), thereby increasing the density of active sites. *In situ* Raman spectra at -1.0 V versus RHE confirmed that the bulk and vast majority of SnS_x is reduced to Sn metal at high potentials ([Figure S5](#)). As discussed later, the catalytic activity of Sn(S)/Au shows significantly superior performance than pure Sn nanoparticles/Au samples, which is in agreement with DFT calculations ([Table 1](#)).

Morphological strategies have been shown to dramatically increase the rate for CO₂RR toward a given product. Field-induced reagent concentration (FIRC) is a catalytic phenomenon that was first reported on nanostructured gold nanoneedles for the reduction of CO₂ to CO ([Figure 2A](#)).³ Simply, high-curvature nanostructures exhibit a high local negative electric field, which concentrates proximate positively charged cations that help to stabilize CO₂ reduction intermediates, promoting CO₂RR. Computational studies have since shown that strong local electric fields and the presence of cations proximate to the surface promote CO₂RR.³³ The concept of sharp nanostructures promoting CO₂RR activity and boosting current densities has since been demonstrated for CO₂ reduction to formate¹³ and formic acid oxidation¹⁵ on branched Pd NPs and CO₂ reduction to ethylene on copper nanodendrites.¹⁷

We sought to explore the synergy between FIRC and sulfur-modulated tin catalysts, building hybrid electrodes that combine the best nanostructured FIRC morphologies of Au nanoneedles with Sn(S), which improves formate evolution energetics ([Figure 2](#)). This required that the sulfur-modulated tin film be conformally deposited over the Au nanoneedles, maximizing activity toward the desired products and otherwise blocking CO active Au facets. We optimized the ALD process by controlling substrate preparation, pulse duration, and the number of cycles ([Figures 2B and 2D](#)). We achieved homogeneously dispersed sulfur elements into the Sn metal by ALD of SnS_x followed by an *in situ* reduction process to give the active Sn(S) catalyst ([Figures 2C and 2E](#)). We have found that regardless of starting Sn:S composition (1:1 or 1:2), the majority of the sulfur is removed during the reduction step. These results imply a limitation to the amount of sulfur that can remain after the initial reduction to SnS_x ([Figure S13](#)).

High-resolution transmission electron microscopy (HRTEM) studies were performed to provide greater insight into the surface structure and morphology of the catalyst

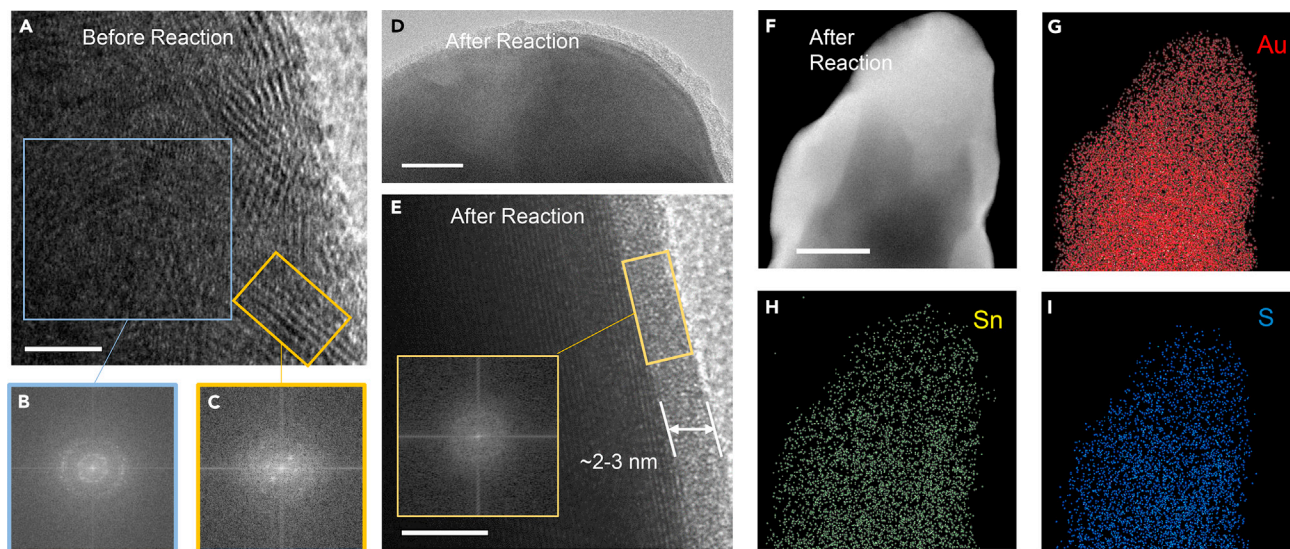


Figure 3. Characterization of Sulfur-Modulated Tin Catalysts

(A) High-resolution transmission electron microscope (HRTEM) image of the ALD Sn_x before reaction showing a highly polycrystalline surface. Scale bar represents 5 nm.

(B and C) Fast Fourier transform (FFT) of the polycrystalline region (B) and one specific crystalline grain (C).

(D and E) HRTEM image of the reduced Sn(S) active catalyst after reaction showing a uniform amorphous layer on the surface. Scale bar represents 20 nm for (D); scale bar represents 5 nm for (E). Inset is the FFT of the amorphous region.

(F–I) STEM image (F) of Sn(S)/Au and the corresponding EDS mapping to show homogeneously dispersed Au (G), Sn (H), and S (I). Scale bar represents 100 nm.

before and after reaction (Figure 3). It was found that, before reaction, highly polycrystalline tin sulfide is formed with extremely small grain sizes of ~5 nm (Figures 3A–3C). After reaction, a thin layer of amorphous tin-based material about 2–3 nm thick forms on the surface (Figures 3D and 3E). Scanning transmission electron microscopy-energy dispersive spectroscopy (STEM-EDS) elemental mapping showed a conformal coating of Sn(S) on Au needles, and a uniform, uncorrelated spatial distribution of Au, Sn, and S (Figures 3F–3I), consistent with the EDS line scan (Figure S6).

To elucidate the electronic configuration of the resulting Sn(S) layer in the final structure, we performed X-ray absorption spectroscopy (XAS) on Sn(S) and Sn NPs before, *in situ*, and after reaction (Figure 4). Sn NPs were used as a control of Sn(S). We analyzed the edge position of each compound as it shifts to higher energies with increasing oxidation of Sn.^{34,35} *In situ* Sn L₃-edge spectra at –0.7 V versus RHE indicate that the reduction of SnS_x to Sn(S) resulted in an oxidation state between Sn⁰ and Sn²⁺, while Sn NPs do not change oxidation state (Figure 4A).^{36,37} This suggests Sn(S) at –0.7 V versus RHE was more oxidized than Sn metal, which agreed with the *in situ* S K-edge spectra³⁸ (Figure S11). The trend observed from the Sn L₃-edge (Figure 4B) indicates that sulfur-doped Sn possessed a higher oxidation state than Sn NPs after reaction (edge shift indicated by a red arrow),^{36,37} consistent with Sn K-edge measurements (Figure 4C).³⁵ Sn(S) exhibited a higher oxidation state than Sn NPs after reaction because Sn(S) was more readily oxidized to high valence after exposure to the open circuit potential and air. We propose that Sn(S) may have more undercoordinated Sn sites than the Sn NP control.

The surface chemical compositions of SnS_x, Sn(S) after reaction, and Sn NPs after reaction were further probed by X-ray photoelectron spectroscopy (XPS). The S 2p spectra of Sn(S) after reaction revealed the survival of sulfur throughout the reaction (Figure 4D). Based on the results from XPS analysis, the content of S in the Sn(S)

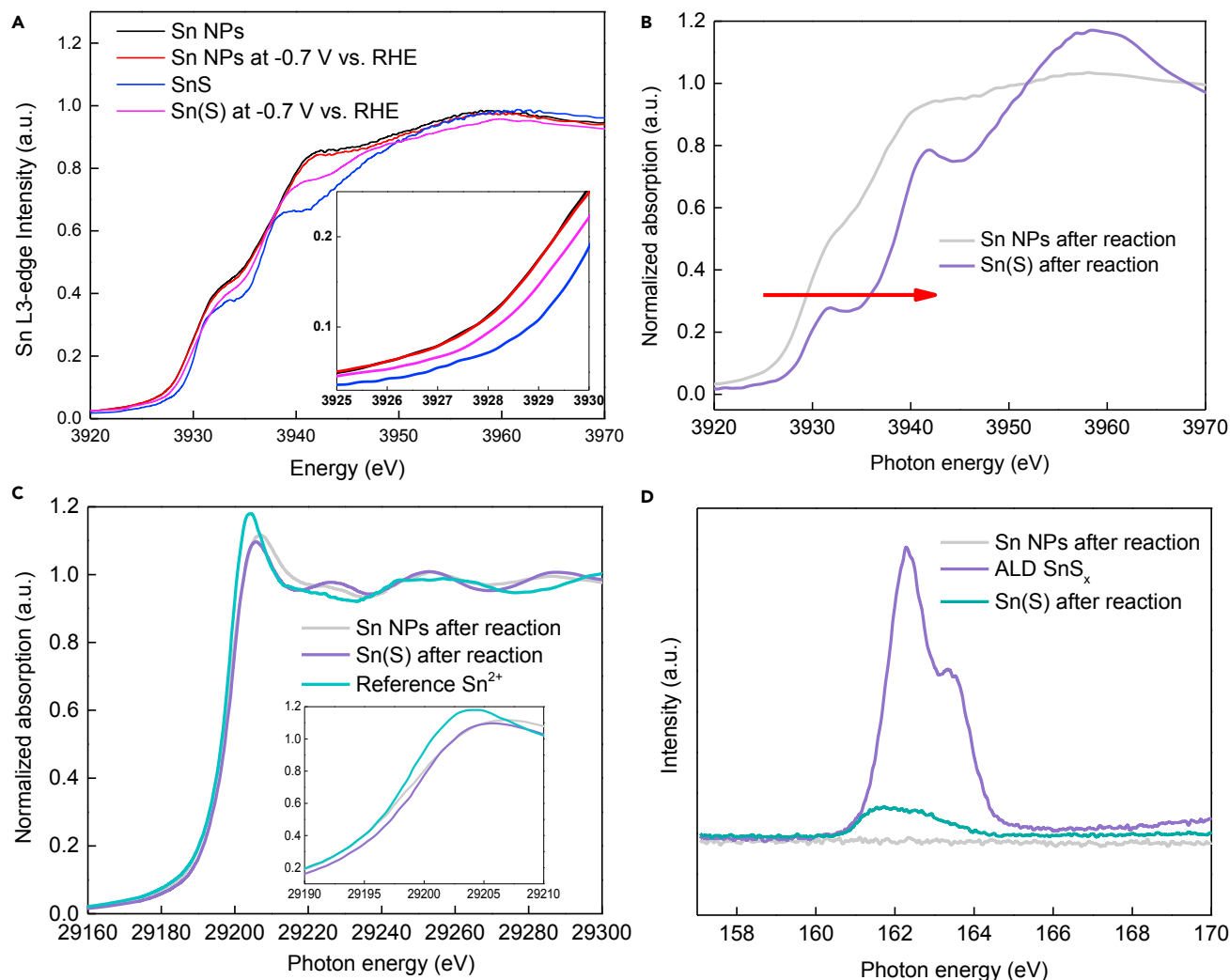


Figure 4. Electronic Structure of Sn(S) and Sn

(A) *In situ* Sn L₃-edge XANES spectra of Sn NPs, SnS, Sn NPs at -0.7 V versus RHE, and Sn(S) at -0.7 V versus RHE. Inset shows zoom in of the pre-edge energy range.

(B) Sn L₃-edge spectra of Sn(S) and Sn NPs on carbon paper after reaction (edge shift indicated by a red arrow).

(C) Sn K-edge of Sn(S) and relevant controls. Inset shows zoom in of the pre-edge energy range.

(D) XPS spectra of Sn(S), Sn NPs, and ALD SnS_x.

catalyst was calculated to be 3.2 at %. To avoid the effect of Au substrates and thus the potential increased sulfur content adhering to gold, we deposited Sn(S) on carbon paper (Figure S14) and found the content of S in the Sn(S)/carbon paper after reaction to be 4.6% (Figure S15).

Evaluation of Activity for Electrochemical Reduction of CO₂

We then proceeded to evaluate the catalytic performance of the Sn(S)-FIRC hybrid electrodes. Linear sweep voltammetry traces reveal the superior current density of S-modulated Sn samples over bare Sn NPs (Figure 5A). The Faradaic efficiency of S-modulated Sn samples approaches 100% for potentials more negative than -600 mV versus RHE. The resulting partial current density is significantly higher than that of Sn samples (Figures 5B and S12). We have also synthesized Sn film on Au needles by sputtering as a control (Figure S19). A record Faradaic efficiency of 93%

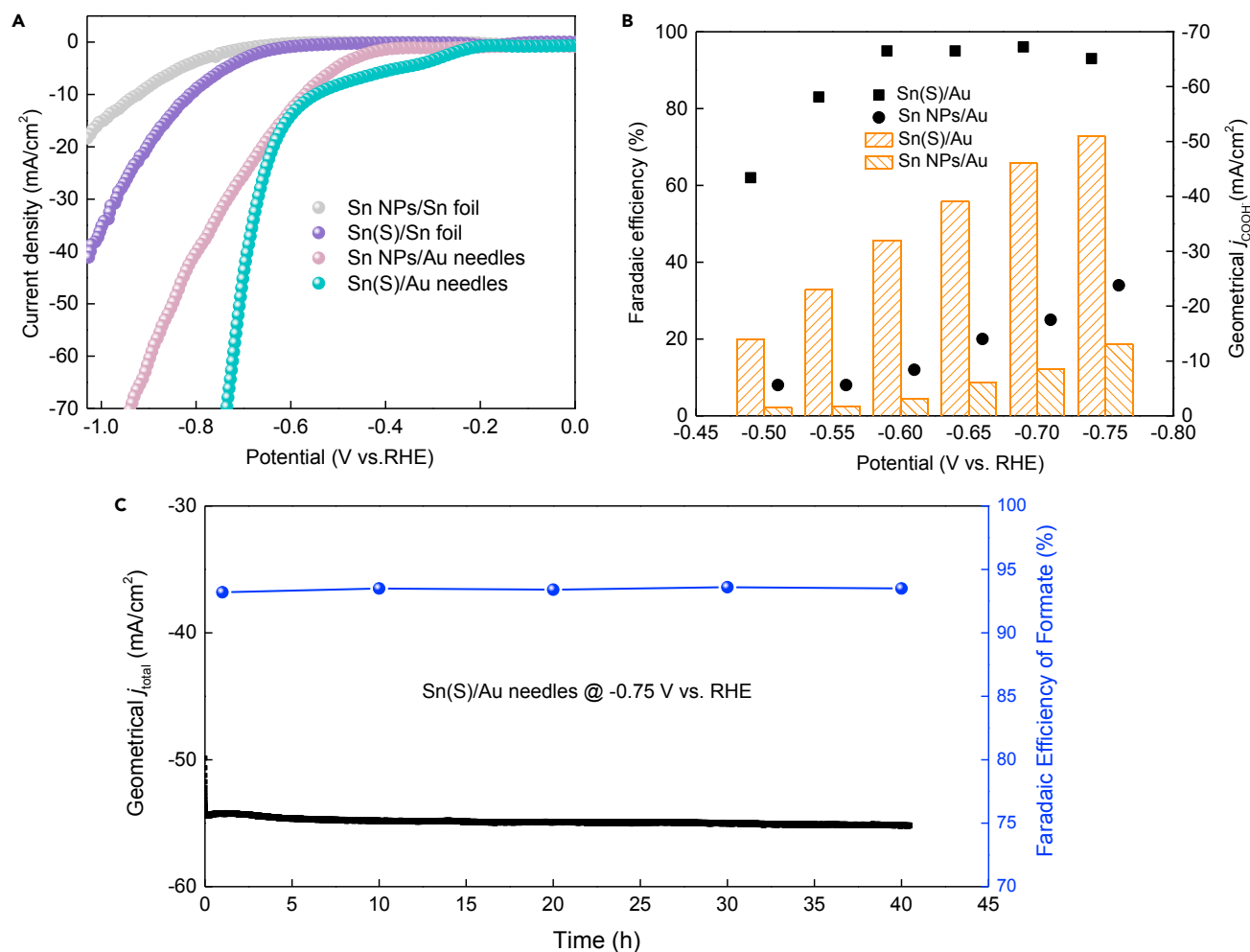


Figure 5. Performance of Sulfur-Modulated Tin Catalysts and Controls in a Three-Electrode Configuration in CO₂ Saturated 0.1 M KHCO₃ Aqueous Electrolyte

(A) The CO₂RR polarization curve of catalysts loaded on Au needles and Sn foil, respectively.

(B) Potential dependence (with iR corrected) of Faradaic efficiencies and current densities for CO₂RR on Sn(S)/Au (squares) and Sn NPs/Au (circles).

(C) Stability test of Sn(S) at -0.75 V versus RHE (iR corrected).

with a total current density of 55 mA cm⁻² (normalized to geometric surface area) is obtained at -0.75 V versus RHE for Sn(S)/Au. This formate partial current density on Sn(S)/Au represents higher than that of the best non-noble metal (Tables 1 and S8). To evaluate the effect of surface area, we measured the ECSA for Sn(S)/Au, Sn NPs/Au, and sputtered Sn/Au from the electrochemical double-layer capacitance of the catalytic surface (Figure S8). From ECSA normalized performance of CO₂ reduction to formate, the high catalytic activity of Sn(S)/Au includes an appreciable intrinsic (not surface-area-related) contribution. The partial current density for formate on Sn(S)/Au, normalized by ECSA, is between 1.2 and 3 times higher than that of Sn NPs/Au and sputtered Sn/Au (Figure S9 and Table S9). To experimentally probe the reaction intermediates, we observed formate in the interfacial region (1,300–1,400 cm⁻¹) by *in situ* attenuated total reflection mode Fourier transform infrared (ATR-FTIR) (Figure S18).^{39,40} We note that a bound intermediate formate species (HCOO*) has been reported before in the literature,³⁹ but unfortunately we were not able to detect this species. While our *in situ* ATR-FTIR was inconclusive for bound HCOO* intermediates, there were no peaks that could be attributed to

the bound or interfacial carboxylate intermediate (COOH*). These results qualitatively agree well with our simulations, whereby the reaction pathways are based on prior literature.^{13,25}

One of the most critical aspects of formate production from CO₂RR is the deactivation of the catalyst over time. Although Pd catalysts only require low potential for CO₂ to formate (Table 1), CO poisoning has limited its potential practical application.¹³ To characterize the performance stability of the Sn(S) catalysts, we performed CO₂ reduction with the Sn(S) catalyst under a constant potential of −0.75 V versus RHE continuously for 40 hours. We observed no appreciable decrease (<2%) in current (Figure 5C) during this time interval. Furthermore, we performed potential-cycling experiments that showed no degradation in activity over five 1-hr cycles (Figure S20). We also confirmed the Faradaic efficiency for formate generation was nearly quantitative (>93%) throughout the electrocatalytic process. This formate partial current density on Sn(S)/Au is higher than the previously reported non-noble metal catalysts in aqueous solution (Table 1),^{2,30} confirming that the undercoordinated tin sites greatly increased the catalytic activity of CO₂ to formate.

EXPERIMENTAL PROCEDURES

DFT Calculations

Initially, we started by simulating a SnS slab.⁴¹ It is characterized by an orthorhombic herzenbergite structure where the Sn²⁺ ion adopts a tetrahedral geometry coordinating three S^{2−} ions with the Sn 5s² lone pair occupying the fourth position.⁴² We then gradually increased the Sn content in the SnS crystal structure by randomly replacing S atoms with Sn atoms such that the resultant structures had 37.5%, 25%, and 12.5% sulfur content. The atomic positions and unit cell parameters of all structures were relaxed and fully optimized using DFT (Figure S17). The optimized structural parameters for SnS (Tables S1 and S2) served as a benchmark for the validity of further calculations. The {100} facet was used for all slabs with a 4 × 4 × 4 atom slab and 20 Å between mirror images in the z axis in the unit cell. To justify the facet choice, we calculated the surface energies for the {100}, {110}, {111}, {211}, and {311} facets of SnS (Table S7). It was found that the {100} facet has the lowest surface energy and is thus expected to be the most stable surface. Bader charge analysis shows electron density of the bound oxygen atoms is slightly higher on slightly doped Sn(S), suggesting a stronger Sn–O intermediate bond (Table S5).

X-Ray Absorption Measurements

The Sn K-edge spectra were collected at the 06ID-1 Hard X-ray MicroAnalysis (HXMA) beamline and soft X-ray Microcharacterization (SXMRB) beamline from Canadian Light Source. *In situ* Sn-L₃ edge and S K-edge XANES spectra were collected at the soft X-ray Microcharacterization (SXMRB) beamline from Canadian Light Source. *Ex situ* Sn L₃-edge spectra were collected at Beamline 10.3.2 from the Advanced Light Source.

Preparation of Sn(S) on Au Needles

Gold electrodes were prepared through an electrodeposition process using a solution containing HAuCl₄ (99.99%, Sigma) and HCl (TraceSELECT) solution.³ SnS_x was deposited at 90°C using tetrakis(dimethylamino)-tin(IV) (TDMASn, 99.99% Sn; Strem Chemicals) and H₂S at a constant growth rate of 0.035 nm per cycle measured by ellipsometry. TDMASn was held at 65°C. Nitrogen was used as a carrier gas (99.9999% pure, Carbagas) with a flow rate of 10 sccm.^{43–45} Cyclic voltammetry measurements from 0.4 V to −1.0 V versus RHE at 50 mV/s were performed in CO₂ saturated 0.1 M KHCO₃ electrolyte for three cycles to activate and partially remove sulfur atoms from

the as-prepared SnS_x/Au electrode. The CO₂ reduction performance was then carried out in the same electrolyte.

Preparation of Sn Nanoparticles on Au Needles

Electrophoretic deposition was implemented to uniformly deposit Sn NPs on nanostructured Au electrode.^{34,46,47} Specially, 10 mg/L Sn NPs in ethanol were placed in the ultrasonic bath for 50 min and centrifuged for 30 min at 4,000 rpm to remove large NPs from the suspension. Finally, a DC power supply of 20 V was applied for 20 min to deposit Sn NPs (Figure S7).

Electrocatalytic Reduction of CO₂

All CO₂ reduction experiments were performed using a three-electrode system connected to an electrochemical workstation (Autolab PGSTAT302N). Ag/AgCl (with saturated KCl as the filling solution) and platinum mesh were used as reference and counter electrodes, respectively. Electrode potentials were converted to the RHE reference scale using $E_{\text{RHE}} = E_{\text{Ag/AgCl}} + 0.197 \text{ V} + 0.0591 \times \text{pH}$. The potentials were iR corrected using electrochemical impedance spectroscopy (Figure S16).

The electrolyte was 0.1 M KHCO₃ saturated with CO₂. Formate was quantified on gas chromatography with mass spectrometry (PerkinElmer Clarus 600 GC-MS System). Assuming that two electrons are needed to produce one formate molecule, the Faradaic efficiency was calculated as follows: Faradaic efficiency = $2F \times n_{\text{formate}}/Q = 2F \times n_{\text{formate}}/(I \times t)$, where F is the Faraday constant, I is the current, t is the running time, and n_{formate} is the total amount of formate produced (in moles).

Characterization

High-resolution TEM (HRTEM) images were taken on an FEI monochromated F20 UT Tecnai microscope operated at 200 kV. STEM elemental mapping of samples were taken on a FEI Titan 80–300 environmental (scanning) electron microscope (E(S) TEM), with a spot size of 6 and a C2 aperture size of 70 μm. Scanning electron microscopy (SEM) was performed on a Hitachi SU8230 scanning electron microscope operated at 1.0 kV. Powder X-ray diffraction patterns were obtained with a MiniFlex600 instrument. XPS measurements were carried out on a Thermo Scientific K-Alpha system, with a 300 μm spot size, 75 eV pass energy, and energy steps of 0.05 eV, and aluminum anode X-ray excitation. The Shirley algorithm was used to fit the background. Then the atomic ratio was computed by summing over the curves over the background and taking into account the absorption cross-section of Sn and S to determine relative ratios from their intensities (Figure S10). The *in situ* spectroelectrochemical (ATR-FTIR) measurements were performed on a Bruker IFS 66/S spectrometer. For the *in situ* technique, a sealed electrochemical cell (Figure S18) with Pt as counter electrode, Sn(S) as working electrode, and Ag/AgCl reference electrode was mounted in the spectrometer. The system was continuously flushed with CO₂ saturated 0.1 M KHCO₃. Sn(S) was deposited onto a germanium crystal (1 × 1 × 0.2 cm parallelepiped, angle 45°C) as reflection element. During the spectroscopic recording, a constant potential was applied (−0.3 V, −0.5 V, and −0.7 V versus RHE, respectively) (Figure S18).

SUPPLEMENTAL INFORMATION

Supplemental Information includes Supplemental Experimental Procedures, 20 figures, and 9 tables and can be found with this article online at <https://doi.org/10.1016/j.joule.2017.09.014>.

AUTHOR CONTRIBUTIONS

E.H.S. and P.Y. supervised the project. X.Z. designed the experiments. P.D.L. carried out the simulation parts. X.Z., P.D.L., N.B., and M.N.B. performed the X-ray measurements. M.B.R. carried out *in situ* Raman measurements. Yifan Li and Yuzhang Li performed the TEM measurements. O.V. carried out the XPS measurements. X.Z., F.P.G.d.A., B.Z., M.L., T.Z., and C.T.D. performed electrochemical measurements. P.S. carried out *in situ* FTIR measurements. Y.C. and X.D. revised the manuscript. All authors discussed the results and assisted during manuscript preparation.

ACKNOWLEDGMENTS

This work was supported by the Ontario Research Fund - Research Excellence Program (RE08-034); NSERC (RGPIN-2017-06477); and the CIFAR Bio-Inspired Solar Energy program (FL-000560). This work was also supported by the Director, Office of Science, Office of Basic Energy Sciences, Chemical Sciences, Geosciences, & Biosciences Division, of the U.S. Department of Energy under contract no. DE-AC02-05CH11231, FWP no. CH030201 (Catalysis Research Program), National Basic Research Program of China (2014CB931703), and the Natural Science Foundation of China (51471115, 51571149). X.Z. acknowledges a scholarship from the China Scholarship Council (CSC) (20140625004). P.D.L. acknowledges NSERC for financial support in the form of the Canada Graduate Scholarship – Doctoral (CGS-D). The CLS is supported by the Natural Sciences and Engineering Research Council of Canada, the National Research Council Canada, the Canadian Institutes of Health Research, the Province of Saskatchewan, Western Economic Diversification Canada, and the University of Saskatchewan. The authors thank Y.J. Pang, J. Li, and Z.Q. Zhang for fruitful discussions, R. Wolowiec and D. Kopilovic for their help during the course of study. DFT computations were performed using the IBM BlueGene/Q supercomputer at the SciNet HPC Consortium provided through the Southern Ontario Smart Computing Innovation Platform (SOSCIP). We acknowledge M. Marcus and the use of Beamline 10.3.2 at the Advanced Light Source for collection of XAS data. The Advanced Light Source and Molecular Foundry are supported by the Director, Office of Science, Office of Basic Energy Sciences, of the U.S. Department of Energy under contract no. DE-AC02-05CH11231.

Received: June 17, 2017

Revised: August 19, 2017

Accepted: September 25, 2017

Published: October 16, 2017

REFERENCES

1. Lin, S., Diercks, C.S., Zhang, B., Kornienko, N., Yang, P., and Yaghi, O.M. (2015). Covalent organic frameworks comprising cobalt porphyrins for catalytic CO₂ reduction in water. *Science* 349, 1208–1215.
2. Mccollum, D.L., Jewell, J., Krey, V., Ramanathan, V., Fay, M., and Riahi, K. (2016). Quantifying uncertainties influencing the long-term impacts of oil prices on energy markets and carbon emissions. *Nat. Energy* 1, 1–7.
3. Liu, M., Pang, Y., Zhang, B., De Luna, P., Voznyy, O., Xu, J., Zheng, X., and Sargent, E. (2016). Enhanced electrocatalytic CO₂ reduction via field-induced reagent concentration. *Nature* 537, 382–386.
4. Gao, S., Lin, Y., Jiao, X., Sun, Y., Luo, Q., and Zhang, W. (2016). Partially oxidized atomic cobalt layers for carbon dioxide electroreduction to liquid fuel. *Nature* 529, 68–71.
5. Benson, E.E., Kubiak, C.P., Sathrum, A.J., and Smieja, J.M. (2009). Electrocatalytic and homogeneous approaches to conversion of CO₂ to liquid fuels. *Chem. Soc. Rev.* 38, 89–99.
6. Li, C.W., Ciston, J., and Kanan, M.W. (2014). Electroreduction of carbon monoxide to liquid fuel on oxide derived nanocrystalline copper. *Nature* 508, 504–507.
7. Goepfert, A., Czaun, M., Jones, J.P., Surya Prakash, G.K., and Olah, G.A. (2014). Recycling of carbon dioxide to methanol and derived products - closing the loop. *Chem. Soc. Rev.* 2, 189–194.
8. Reda, T., Plugge, C.M., Abram, N.J., and Hirst, J. (2008). Reversible interconversion of carbon dioxide and formate by an electroactive enzyme. *Proc. Natl. Acad. Sci. USA* 105, 10654–10658.
9. Wang, W., Hameda, Y., Muckerman, J., and Fujita, E. (2015). CO₂ hydrogenation to formate and methanol as an alternative to photo- and electrochemical CO₂ reduction. *Chem. Rev.* 115, 12936–12973.
10. Verma, S., Kim, B., Jhong, H.R., Ma, S., and Kenis, P.J. (2016). A gross-margin model for defining technoeconomic benchmarks in the

- electroreduction of CO₂. *ChemSusChem* 9, 1972–1979.
11. Lu, X., Leung, D.Y.C., Wang, H., Leung, M.K.H., and Xuan, J. (2014). Electrochemical reduction of carbon dioxide to formic acid. *ChemElectroChem* 1, 836–849.
 12. Chen, Y., and Kanan, M.W. (2012). Tin oxide dependence of the CO₂ reduction efficiency on tin electrodes and enhanced activity for tin/tin oxide thin-film catalysts. *J. Am. Chem. Soc.* 134, 1986–1989.
 13. Klinkova, A., De Luna, P., Dinh, C.T., Voznyy, O., Larin, E., and Kumacheva, E. (2016). Rational design of efficient palladium catalysts for electroreduction of carbon dioxide to formate. *ACS Catal.* 6, 8115–8120.
 14. Kim, D., Resasco, J., Yu, Y., Asiri, A.M., and Yang, P. (2014). Synergistic geometric and electronic effects for electrochemical reduction of carbon dioxide using gold-copper bimetallic nanoparticles. *Nat. Commun.* 5, 4948.
 15. Zhang, S., Kang, P., and Meyer, T.J. (2014). Nanostructured tin catalysts for selective electrochemical reduction of carbon dioxide to formate. *J. Am. Chem. Soc.* 136, 1734–1737.
 16. Lee, S., Kim, D., and Lee, J. (2015). Electrocatalytic production of C3-C4 compounds by conversion of CO₂ on a chloride-induced bi-phasic Cu₂O-Cu catalysts. *Angew. Chem. Int. Ed.* 127, 14914–14918.
 17. Zhu, Q., Ma, J., Kang, X., Sun, X., Liu, H., and Hu, J. (2016). Efficient reduction of CO₂ into formic acid on a lead or tin electrode using an ionic liquid catholyte mixture. *Angew. Chem. Int. Ed.* 55, 9012–9016.
 18. Won da, H., Choi, C.H., Chung, J., Chung, M.W., Kim, E.H., and Woo, S.I. (2015). Rational design of a hierarchical tin dendrite electrode for efficient electrochemical reduction of CO₂. *ChemSusChem* 8, 3092–3098.
 19. Min, X., and Kanan, M.W. (2015). Pd-catalyzed electrohydrogenation of carbon dioxide to formate: high mass activity at low overpotential and identification of the deactivation pathway. *J. Am. Chem. Soc.* 137, 4701–4708.
 20. Kortlever, R., Peters, I., Koper, S., and Koper, M.T. (2015). Electrochemical CO₂ reduction to formic acid at low overpotential and with high faradaic efficiency on carbon-supported bimetallic Pd–Pt nanoparticles. *ACS Catal.* 5, 3916–3923.
 21. Li, F., Chen, L.P., Knowles, G.R., MacFarlane, D., and Zhang, J. (2016). Hierarchical mesoporous SnO₂ nanosheets on carbon cloth: a robust and flexible electrocatalyst for CO₂ reduction. *Angew. Chem. Int. Ed.* 128, 1–6.
 22. Pander, J.E., Baruch, M.F., and Bocarsly, A.B. (2016). Probing the mechanism of aqueous CO₂ reduction on post-transition-metal electrodes using ATR-IR spectroelectrochemistry. *ACS Catal.* 6, 7824–7833.
 23. Hollingsworth, N., Taylor, S.F., Galante, M.T., Jacquemin, J., Longo, C., Holt, K.B., de Leeuw, N.H., and Hardacre, C. (2015). Reduction of carbon dioxide to formate at low overpotential using a superbase ionic liquid. *Angew. Chem. Int. Ed.* 54, 14164–14168.
 24. Lee, C.H., and Kanan, M.W. (2015). Controlling H⁺ vs CO₂ reduction selectivity on Pb electrodes. *ACS Catal.* 5, 465–469.
 25. Yoo, J.S., Christensen, R., Vegge, T., Nørskov, J.K., and Studt, F. (2016). Theoretical insight into the trends that guide the electrochemical reduction of carbon dioxide to formic acid. *ChemSusChem* 9, 358–363.
 26. Hirunsit, P. (2013). Electroreduction of carbon dioxide to methane on copper, copper silver, and copper–gold catalysts: a DFT study. *J. Phys. Chem. C* 117, 8262–8268.
 27. Rosen, J., Hutchings, G.S., Lu, Q., Rivera, S., Zhou, Y., Vlachos, D.G., and Jiao, F. (2015). Mechanistic insights into the electrochemical reduction of CO₂ to CO on nanostructured Ag surfaces. *Azcs Catal.* 5, 4293–4299.
 28. Mistry, H., Varela, A.S., Bonifacio, C.S., Strasser, P., and Cuenya, B. (2016). Highly selective plasma activated copper catalysts for carbon dioxide reduction to ethylene. *Nat. Commun.* 7, 12123–12130.
 29. Kortlever, R., Shen, J., Schouten, K.J., Calle-Vallejo, F., and Koper, M.T. (2015). Catalysts and reaction pathways for the electrochemical reduction of carbon dioxide. *J. Phys. Chem. Lett.* 6, 4073–4082.
 30. Li, Y., Wang, H., Xie, L., Liang, Y., Hong, G., and Dai, H. (2011). MoS₂ nanoparticles grown on graphene: an advanced catalyst for the hydrogen evolution reaction. *J. Am. Chem. Soc.* 133, 7296–7299.
 31. Li, F., Chen, L., Xue, M., William, T., Zhang, Y.R., and MacFarlane, D. (2017). Towards a better Sn: efficient electrocatalytic reduction of CO₂ to formate by Sn/SnS₂ derived from SnS₂ nanosheets. *Nano Energy* 31, 270–277.
 32. Lei, F., Liu, W., Sun, Y., Xu, J., Liu, K., and Liang, L. (2016). Metallic tin quantum sheets confined in graphene toward high-efficiency carbon dioxide electroreduction. *Nat. Commun.* 7, 12697.
 33. Chen, L.D., Urushihara, M., Chan, K., and Nørskov, J.K. (2016). Electric field effects in electrochemical CO₂ reduction. *ACS Catal.* 6, 7133–7139.
 34. Vinson, J., and Rehr, J.J. (2012). Ab initio Bethe-Salpeter calculations of the X-ray absorption spectra of transition metals at the L-shell edges. *Phys. Rev. B* 78, 78–84.
 35. Moreno, M.S., Egerton, R.F., Rehr, J.J., and Midgley, P.A. (2005). Electronic structure of tin oxides by electron energy loss spectroscopy and real-space multiple scattering calculations. *Phys. Rev. B* 71, 035103.
 36. Liu, Z., Handa, K., Kaibuchi, K., Tanaka, Y., and Kawai, J. (2004). Comparison of the Sn L edge X-ray absorption spectra and the corresponding electronic structure in Sn, SnO, and SnO₂. *J. Electron Spectros. Relat. Phenomena* 135, 155–158.
 37. Vinson, J., Kas, J.J., Vila, F.D., Rehr, J.J., and Shirley, E.L. (2012). Theoretical optical and x-ray spectra of liquid and solid H₂O. *Phys. Rev. B* 85, 045101.
 38. Kapilashrami, M., Kronawitter, C.X., Torndahl, T., Lindahl, J., Hultqvist, A., and Wang, W.C. (2012). Soft X-ray characterization of Zn_(1-x)Sn_(x)O_(y) electronic structure for thin film photovoltaics. *Phys. Chem. Chem. Phys.* 14, 10154–10159.
 39. Baruch, M.F., Pander, J.E., III, White, J.L., and Bocarsly, A.B. (2015). Mechanistic insights into the reduction of CO₂ on tin electrodes using in situ ATR-IR spectroscopy. *ACS Catal.* 5, 3148–3156.
 40. Figueiredo, M.C., Ledezma-Yanez, I., and Koper, M.T. (2016). In situ spectroscopic study of CO₂ electroreduction at copper electrodes in acetonitrile. *ACS Catal.* 6, 2382–2392.
 41. Burton, L.A., and Walsh, A. (2012). Phase stability of the Earth-abundant tin sulfides SnS, SnS₂, and Sn₂S₃. *J. Phys. Chem. C* 116, 24262–24267.
 42. Klimm, K.C., Kohn, S.A., O'Dell, L.E., Botcharnikov, R.E., and Smith, M. (2012). The dissolution mechanism of sulphur in hydrous silicate melts. I: assessment of analytical techniques in determining the sulphur speciation in iron-free to iron-poor glasses. *Chem. Geol.* 322, 237–249.
 43. Wang, D., Yang, J., Liu, J., Li, X., Li, R., and Cai, M. (2014). Atomic layer deposited coatings to significantly stabilize anodes for Li ion batteries: effects of coating thickness and the size of anode particles. *J. Mater. Chem. A* 2, 2306.
 44. Sun, Y., Sun, Z., Gao, S., Cheng, H., Liu, Q., and Lei, F. (2014). All-surface-atomic-metal chalcogenide sheets for high-efficiency visible-light photoelectrochemical water splitting. *Adv. Energy Mater.* 4, 1300611–1300622.
 45. Dasgupta, N.P., Meng, X., Elam, J.W., and Martinson, A.B. (2015). Atomic layer deposition of metal sulfide materials. *Acc. Chem. Res.* 48, 341–348.
 46. Wang, G.J., and Chou, S.W. (2010). Electrophoretic deposition of uniformly distributed TiO₂ nanoparticles using an anodic aluminum oxide template for efficient photolysis. *Nanotechnology* 21, 115206.
 47. Besra, L., and Liu, M. (2007). A review on fundamentals and applications of electrophoretic deposition (EPD). *Progr. Mater. Sci.* 52, 1–61.